

# Quadrupole collectivity in neutron-deficient Sn nuclei: $^{104}\text{Sn}$ and the role of proton excitations

V. M. Bader,<sup>1,2</sup> A. Gade,<sup>1,2</sup> D. Weisshaar,<sup>1</sup> B. A. Brown,<sup>1,2</sup> T. Baugher,<sup>1,2</sup> D. Bazin,<sup>1</sup> J. S. Berryman,<sup>1</sup> A. Ekström,<sup>1,3</sup> M. Hjorth-Jensen,<sup>1,2,3</sup> S. R. Stroberg,<sup>1,2</sup> W. B. Walters,<sup>4</sup> K. Wimmer,<sup>1,5</sup> and R. Winkler<sup>1,\*</sup>

<sup>1</sup>*National Superconducting Cyclotron Laboratory, Michigan State University, East Lansing, Michigan 48824, USA*

<sup>2</sup>*Department of Physics and Astronomy, Michigan State University, East Lansing, Michigan 48824, USA*

<sup>3</sup>*Department of Physics and Center of Mathematics for Applications, University of Oslo, N-0316 Oslo, Norway*

<sup>4</sup>*Department of Chemistry and Biochemistry, University of Maryland, College Park, Maryland 20742, USA*

<sup>5</sup>*Department of Physics, Central Michigan University, Mt. Pleasant, Michigan 48859, USA*

(Dated: October 22, 2018)

We report on the experimental study of quadrupole collectivity in the neutron-deficient nucleus  $^{104}\text{Sn}$  using intermediate-energy Coulomb excitation. The  $B(E2; 0_1^+ \rightarrow 2_1^+)$  value for the excitation of the first  $2^+$  state in  $^{104}\text{Sn}$  has been measured to be  $0.180(37) e^2b^2$  relative to the well-known  $B(E2)$  value of  $^{102}\text{Cd}$ . This result disagrees by more than one sigma with a recently published measurement [1]. Our result indicates that the most modern many-body calculations remain unable to describe the enhanced collectivity below mid-shell in Sn approaching  $N = Z = 50$ . We attribute the enhanced collectivity to proton particle-hole configurations beyond the necessarily limited shell-model spaces and suggest the asymmetry of the  $B(E2)$ -value trend around mid-shell to originate from enhanced proton excitations across  $Z = 50$  as  $N = Z$  is approached.

One of the overarching goals of nuclear physics is the development of a comprehensive model of the atomic nucleus with predictive power across the nuclear chart. While the structure of nuclei close to stability is fairly well understood, significant modifications compared to stable nuclei have been observed for short-lived rare isotopes with unbalanced numbers of protons and neutrons. The driving forces behind these structural changes are manifold, including spin-isospin parts of the nuclear interaction [2] and various facets of many-body correlations [3]. Of particular importance for the development of nuclear models is experimental data that consistently tracks the effect of isospin and changed binding, for example. The chain of Sn isotopes has been a formidable testing ground for nuclear models as some spectroscopic data is available from  $N = Z = 50$   $^{100}\text{Sn}$  [4] in the proximity of the proton drip-line to  $^{134}\text{Sn}$  [5], beyond the very neutron-rich doubly-magic nucleus  $^{132}\text{Sn}$  [6]. In even-even nuclei, the electromagnetic  $B(E2 \uparrow) = B(E2; 0_1^+ \rightarrow 2_1^+)$  excitation strength is a measure of quadrupole collectivity, sensitive to the presence of shell gaps, nuclear deformation, and nucleon-nucleon correlations, for example. In the Sn isotopes, this transition strength has been reported from  $^{104}\text{Sn}$  to  $^{130}\text{Sn}$ , spanning a chain of 14 even-even Sn isotopes. The trend is asymmetric with respect to mid-shell and not even the largest-scale shell-model calculations have been able to describe the evolution of transition strength across the isotopic chain without varying effective charges. In this work, we report the determination of the  $^{104}\text{Sn}$   $B(E2)$  value from intermediate-energy Coulomb excitation with the collision impact parameter restricted to exclude nuclear contributions. Our value exceeds the recently published result [1] and – continuing the trend below mid-shell – is found at variance with the largest-scale shell model cal-

culations. We arrive at a very different conclusion from [1] and explain the enhanced collectivity for neutron-deficient Sn nuclei by considering proton particle-hole intruder configurations observed in neighboring nuclei and  $\alpha$  correlations towards  $N = Z$ . It is suggested that the interplay of proton intruder configurations and quadrupole collectivity is a common phenomenon along proton-magic isotope chains.

The measurement was performed at the National Superconducting Cyclotron Laboratory (NSCL) at Michigan State University. The secondary projectile beam containing  $^{104}\text{Sn}$  and  $^{102}\text{Cd}$  was produced by fragmentation of a 140 MeV/u  $^{124}\text{Xe}$  stable primary beam on a 240 mg/cm<sup>2</sup>  $^9\text{Be}$  production target and separated using a 150 mg/cm<sup>2</sup> Al wedge degrader in the A1900 fragment separator [7]. Despite the total momentum acceptance of the separator being restricted to 0.41%, the  $^{104}\text{Sn}$  purity was only 0.006%. The high levels of contamination originate from low momentum tails of higher rigidity fragments that extend exponentially and overlap with the momentum acceptance of the fragment separator [8]. Therefore, NSCL's Radio Frequency Fragment Separator (RFFS) was used for additional filtering. Using the time micro structure of the accelerated beam, it deflects beam particles according to their time-of-flight with a transverse Radio Frequency field, effectively leading to a phase filtering [9]. The RFFS was tuned to deflect and block part of the main contaminants, increasing the  $^{104}\text{Sn}$  purity in the beam cocktail by two orders of magnitude. At the experimental end station downstream of the RFFS, the resulting rare-isotope beam was composed of 1.25%  $^{104}\text{Sn}$  and 2.9%  $^{102}\text{Cd}$  at average rates of 10 and 26 particles per second, for  $^{104}\text{Sn}$  and  $^{102}\text{Cd}$  respectively.

About 12.8 m downstream from the RFFS, the secondary beam interacted with a gold target of 184 mg/cm<sup>2</sup>

thickness surrounded by the high-efficiency CsI(Na) scintillator array (CAESAR) [10] for in-beam  $\gamma$ -ray spectroscopy. CAESAR was read out in coincidence with a Phoswich detector for particle identification located 0.96 m downstream of the gold target. CAESAR consists of 192 CsI(Na) crystals with about 95% solid-angle coverage. The granularity of the array enables event-by-event Doppler reconstruction of  $\gamma$  rays emitted in flight by the scattered projectiles. The  $\gamma$ -ray detection efficiency of the array was determined with  $^{88}\text{Y}$ ,  $^{22}\text{Na}$ ,  $^{137}\text{Cs}$ ,  $^{133}\text{Ba}$  and  $^{60}\text{Co}$  calibration standards. The measured source spectra and efficiencies agree with GEANT4 simulations which were used to model the in-beam spectral response of CAESAR [11] (30% full-energy peak efficiency at 1 MeV [10]).

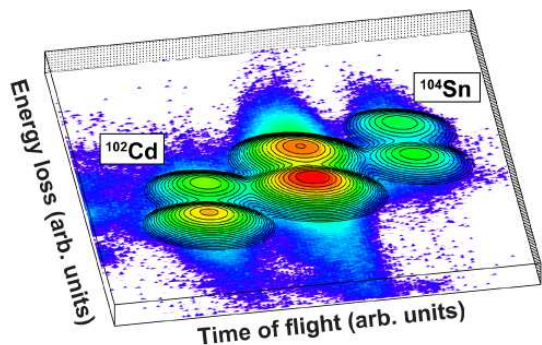


FIG. 1. (Color online) Particle-identification spectrum for the neutron-deficient projectile beam passing through the Au target. The energy loss measured in the PIN detector is plotted versus the ion's flight time.  $^{104}\text{Sn}$  and  $^{102}\text{Cd}$  can be clearly separated. The black lines show two-dimensional Gaussian fits.

The incoming projectiles were identified on an event-by-event basis using energy-loss and time-of-flight measurements. The ion's energy loss was measured with a 300  $\mu\text{m}$  Si PIN detector and the flight time was measured between a plastic scintillator located at the exit of the A1900 and the Phoswich detector downstream of CAESAR. The identification is shown in Fig. 1.

In intermediate-energy Coulomb excitation [12–14], projectiles are scattered off stable high- $Z$  targets and detected in coincidence with the de-excitation  $\gamma$  rays, tagging the inelastic process. Peripheral collisions are selected in the regime of intermediate beam energies to exclude nuclear contributions to the otherwise purely electromagnetic excitation process. This is typically accomplished by restricting the data analysis to events at very forward scattering angles, corresponding to large impact parameters,  $b > b_{min} = 1.25 \text{ fm}(A_p^{1/3} + A_t^{1/3}) + 2 \text{ fm}$ , in the interaction between projectile and target nuclei [14]. This gives maximum scattering angles of  $\theta_{lab}^{max} = 3.126^\circ$  and  $3.206^\circ$  for  $^{104}\text{Sn}$  (67 MeV/u mid-target energy) and  $^{102}\text{Cd}$  (64 MeV/u mid-target energy), respectively. Assuming the reaction happens at the beginning of the tar-

get, at higher beam energies, maximum scattering angles of  $\theta_{lab}^{max} = 2.756^\circ$  and  $2.821^\circ$  for  $^{104}\text{Sn}$  and  $^{102}\text{Cd}$  result. The data analysis in this work was restricted to  $\theta_{lab}^{max} = 2.578^\circ$  for both  $^{104}\text{Sn}$  and  $^{102}\text{Cd}$ , resulting in a conservative minimum impact parameter for both projectiles. Position measurements from a Parallel Plate Avalanche Counter (PPAC), placed between CAESAR and the Phoswich detector, were used to reconstruct each projectile's outgoing angle. The centering of the beam on the PPAC and the focusing on target were carefully adjusted in a dedicated beam tuning period with two PPACs. With the precisely known distance between PPAC and target, the angles were reconstructed from the particle's position on the PPAC. A position uncertainty of 0.5 mm was determined from mask calibrations. This makes the angle measurement based on geometry more precise than the effect of angular straggling estimated to be small <sup>1</sup>. Systematic uncertainties, including the one related to straggling, will divide out in the normalization procedure outlined below.

The event-by-event Doppler-reconstructed  $\gamma$ -ray spectra taken in coincidence with  $^{104}\text{Sn}$  and  $^{102}\text{Cd}$  respectively – with the scattering-angle restrictions applied – are shown in Fig. 2. To improve the peak-to-background ratio, only events with  $\gamma$ -ray multiplicity 1 were considered. In agreement with [16], the  $\gamma$ -ray transition at 1260 keV observed in  $^{104}\text{Sn}$  and the transition at 777 keV in  $^{102}\text{Cd}$  are attributed to the decay of the first  $2^+$  state to the  $0^+$  ground state. No evidence for other transitions was observed.

We would normally determine the absolute angle-integrated Coulomb excitation cross sections,  $\sigma(\theta_{lab} \leq \theta_{lab}^{max})$ , and translate them into absolute  $B(\sigma\lambda)$  excitation strengths using the Winther-Alder description of intermediate-energy Coulomb excitation [17], however, this was not possible here as the absolute efficiencies of this new setup and data acquisition system are not characterized as well as in our work at the S800 spectrograph (see [18], for example). Therefore, the  $B(E2 \uparrow) = B(E2; 0^+ \rightarrow 2_1^+)$  excitation strength for  $^{104}\text{Sn}$  was determined relative to the well known  $B(E2 \uparrow)$  value of  $^{102}\text{Cd}$  [19], which Coulomb excitation yield was measured in the present work at the very same time, under identical conditions, and with good statistics,

$$B(E2 \uparrow)^{Sn} = B(E2 \uparrow)^{Cd} \cdot \frac{N_\gamma^{Sn} N_{proj}^{Cd} AW(Cd)}{N_\gamma^{Cd} N_{proj}^{Sn} AW(Sn)}, \quad (1)$$

<sup>1</sup> We estimated the effect of straggling with a Monte Carlo simulation that assumes  $\sigma = 0.4^\circ$  angular straggling [15]. The input distribution was chosen to match the measured angular distribution when folded with the straggling distribution. For both,  $^{104}\text{Sn}$  and  $^{102}\text{Cd}$ , we determined that for all angles larger than  $1.5^\circ$  about 0.7 to 1.5% of the counts originate from larger scattering angles that fulfill our maximum angle cut since they straggled to smaller angles and we lose about 3-4% of events that would have fulfilled the maximum angle cut without angular straggling.

with  $N_{\gamma}^{Sn,Cd}$  and  $N_{proj}^{Sn,Cd}$  the number of  $2_1^+$  de-excitation  $\gamma$ -rays and projectiles for  $^{104}\text{Sn}$  and  $^{102}\text{Cd}$ , respectively. The term  $AW(Sn,Cd)$  is the Alder-Winther angle-integrated Coulomb excitation cross section,  $\sigma(\theta_{\text{lab}} \leq 2.578^\circ)$  per unit  $B(E2)$  value, for  $^{104}\text{Sn}$  and  $^{102}\text{Cd}$ , respectively, taking into account the proper kinematics and atomic number of the projectiles.

The number of projectiles,  $N_{proj}$ , was determined from the particle identification spectrum shown in Fig. 1. Two-dimensional Gaussian fits, also shown in the figure, were used to estimate the contamination from neighboring, highly intense constituents of the cocktail beam. These corrections to the number of projectiles were below 3% for both  $^{104}\text{Sn}$  and  $^{102}\text{Cd}$ .

The simulated (GEANT4) response of CAESAR was scaled to the  $^{104}\text{Sn}$  and  $^{102}\text{Cd}$  data to determine the number of  $2_1^+$  de-excitations,  $N_{\gamma}$ . The simulations takes into account CAESAR's  $\gamma$ -ray detection efficiency and the absorption in the gold target and surrounding materials and include the calculated  $\gamma$ -ray angular distribution in Coulomb excitation [17, 20]. The simulated response functions fitted on top of a double exponential smooth background are shown in Fig. 2.

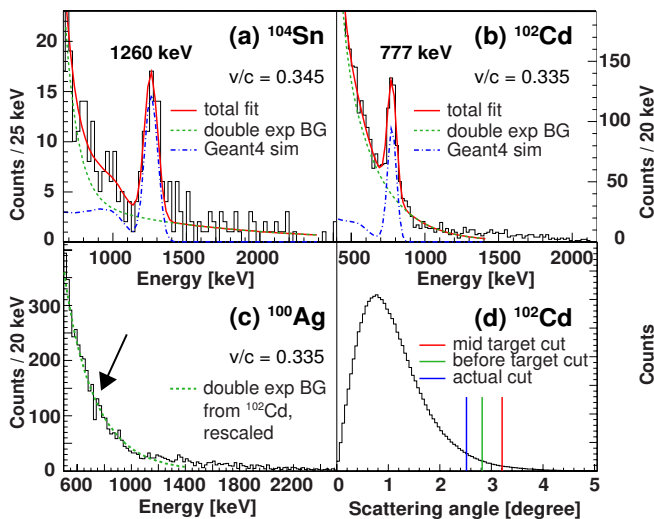


FIG. 2. (Color online) Event-by-event Doppler reconstructed  $\gamma$ -ray spectra detected in coincidence with scattered  $^{104}\text{Sn}$  (a) and scattered  $^{102}\text{Cd}$  (b). Gamma-ray transitions at 1260 keV and 777 keV can be clearly identified and are attributed to the de-excitation  $\gamma$  rays from the first excited  $2_1^+$  state in  $^{104}\text{Sn}$  and in  $^{102}\text{Cd}$ , respectively. (c) shows the  $^{102}\text{Cd}$  background fit scaled to  $^{100}\text{Ag}$  for which no de-excitations are observed in the sensitive region and (d) displays the scattering angle spectrum with our conservative angle cut indicated.

With the known value of  $B(E2 \uparrow) = 0.28(3) e^2b^2$  for  $^{102}\text{Cd}$  [19], we deduce  $B(E2 \uparrow) = 0.180(37) e^2b^2$  for  $^{104}\text{Sn}$ . The uncertainty includes all statistical uncertainties of  $N_{proj}$ , uncertainties from the fits of the response functions used to derive  $N_{\gamma}$  and the uncertainty of the  $^{102}\text{Cd}$   $B(E2 \uparrow)$  value. The aforementioned normaliza-

TABLE I.  $B(E2; 0_1^+ \rightarrow 2_1^+)$  values for  $^{102}\text{Cd}$  and  $^{104}\text{Sn}$  from literature and from this work ( $^{104}\text{Sn}$ ); we used the results from [19] for normalization in eq. (1).

Isotope	$B(E2 \uparrow)_{\text{literature}}$ ( $e^2b^2$ )	Ref	$B(E2 \uparrow)$ ( $e^2b^2$ )
$^{102}\text{Cd}$	0.28(3) <sup>a</sup>	[19]	
	0.281(45)	[22]	
$^{104}\text{Sn}$	0.10(4)	[1]	0.180(37)
	0.163(26)	[21]	

<sup>a</sup> The error includes statistical and systematic uncertainties.

tion eliminates systematic uncertainties stemming from the angle-determination with the PPAC and absolute efficiencies in general. Our result compares well with the work by Doornenbal [21] and disagrees with the recently published value from a relativistic Coulomb excitation measurement performed at GSI [1]. Ref. [21] discusses the impact of unobserved feeding and we point out that,  $^{102}\text{Cd}$  and  $^{104}\text{Sn}$  have rather comparable proton separation energies,  $S_p = 5.614$  MeV and  $S_p = 4.286$  MeV, respectively, with a similar potential of unobserved feeding from higher-lying  $3^-$  and  $2_n^+$  states. Nuclear contributions are minimized in our work by very conservative minimum impact parameters that the analysis is restricted to, avoiding model-dependent estimates of the nuclear contribution. Our results and the literature values are summarized in Table I. An overview of the measured  $B(E2 \uparrow)$  values along the Sn isotopic chain is given in Fig. 3(a).

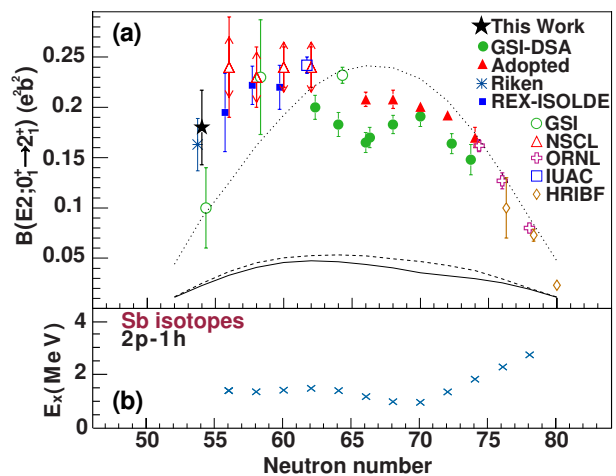


FIG. 3. (Color online) (a) Measured  $B(E2 \uparrow)$  values for the chain of Sn isotopes: Adopted [16], Riken [21], REX-ISOLDE [23, 24], GSI-DSA [25], GSI [1, 26, 27], NSCL [28], ORNL [29], IUAC [30], HRIBF [31]. Solid line: Large-scale shell-model (LSSM) calculations with NNLO interaction [32]. Dashed line: LSSM with  $N^3\text{LO}$  interaction [33]. The dotted line reproduces the gds ( $t_{\pi} = 4$ ) calculation shown in [26]. (b) Energies of the proton  $2p-1h$  intruder states in Sb nuclei [34].

In order to understand the trend in  $B(E2 \uparrow)$  strength toward  $^{100}\text{Sn}$ , we have performed several large-scale shell-model (LSSM) calculations, using a recently parametrized nucleon-nucleon force based on chiral perturbation theory [32] (at next-to-next leading order, NNLO) as well as the  $\text{N}^3\text{LO}$  nucleon-nucleon interaction of [33]. We have also studied the influence of three-body forces following Ref. [35]. We employ  $^{100}\text{Sn}$  as a closed-shell core, defined by the quantum numbers of the  $0h_{11/2}$ ,  $1d$ ,  $2s_{1/2}$  and  $0g_{7/2}$  single-neutron states. One major problem with this model space is that the single-particle energies of  $^{101}\text{Sn}$  are not known experimentally, except for the spacing between the  $7/2_1^+$  and the  $5/2_1^+$  states of 170 keV [36, 37]. The effective neutron charge was set to  $0.5e$  for all calculations.

All of these calculations result in rather similar behaviors for the  $B(E2 \uparrow)$  transitions in the neutron-deficient tin isotopes. In Fig. 3 we thus present only the results for the newly optimized NNLO interaction [32], together with those obtained with the  $\text{N}^3\text{LO}$  interaction [33]. The latter interaction also gives the overall best reproduction of the excited states and binding energies. Thus, unless one adopts a phenomenological adjustment of the effective neutron charges, see for example Ref. [38], theory based on an inert proton core fails to describe the  $B(E2 \uparrow)$  strengths. Our results are similar to the  $t = 0$  results shown in Fig. 3 of [26]. If we increase the neutron effective charge to  $1.0e$ , then the  $B(E2)$  values are increased by a factor of four and are in better agreement with the data. But they are still too small for the neutron-deficient tin isotopes.

In [26], the model space was increased to allow up to four protons to be excited from the  $0g_{9/2}$  orbital to  $1d$ ,  $2s_{1/2}$  and  $0g_{7/2}$ , ( $t_\pi = 4$ ). The results from this calculation, with effective charges  $1.5e$  for protons and  $0.5e$  for neutrons, are also shown in Fig. 3. Overall, the data is much better described, except that the extended calculation is symmetric around the middle, whereas experiment shows an asymmetry with an enhancement at the neutron-deficient end.

In [28], the comparison to data and theory for the nickel isotopes was discussed.  $^{56}\text{Ni}$  and  $^{100}\text{Sn}$  are similar with regard to their structure and shell gaps. At the closed-shell limit, they are both  $jj$  closed shells with the  $0f_{7/2}$  and  $0g_{9/2}$  orbitals filled, respectively. There are low-lying one-particle one-hole ( $1p - 1h$ ) excitations across the shell gap that give a moderately large  $B(E2)$  strength in  $^{56}\text{Ni}$  (experimentally observed in [39]) and  $^{100}\text{Sn}$  (not yet experimentally observed but calculated for Fig. 4 of [1]). These  $1p - 1h$  proton excitations couple coherently to the neutron configurations. The resulting increase in the  $B(E2)$  values could be interpreted in terms of an additional neutron core-polarization charge for a model space that involves only the valence neutrons.

The  $^{100}\text{Sn}$  effective single-particle energy (ESPE) shell gap for the calculations given was about 7.5 MeV (Fig.

2 in [26]). In comparison, the ESPE gap for the calculations used for the nickel isotopes in Fig. 4 of [28] is 7.1 MeV. The correlated gap obtained from the full  $pf$ -shell calculation and from experimental ground-state binding energies of  $^{55,56,57}\text{Ni}$  is 6.4 MeV. The correlated gap for  $^{100}\text{Sn}$  is not known experimentally and the theoretical value is not provided in [26]. The shell gaps obtained with some Skyrme energy-density functionals for  $^{100}\text{Sn}$  are 5.2 MeV (Skx) [40], 5.9 MeV (SLy4) [41] and 5.8 MeV (SkM\*) [42], and for  $^{56}\text{Ni}$  are 4.1 MeV (Skx), 4.8 MeV (SLy4) and 4.7 MeV (SkM\*). Thus, the shell gaps for  $^{56}\text{Ni}$  and  $^{100}\text{Sn}$  are similar.

In contrast to the ( $t_\pi = 4$ ) calculation for tin isotopes that is symmetric around midshell, the equivalent calculation for nickel (Fig. 4 in [28]) shows an asymmetry with larger  $B(E2)$  values at the neutron-deficient end. For nickel, it is possible to carry out a full  $pf$  shell calculation and this enhances the asymmetry. It is likely that the origin of the difference between the calculations for nickel and tin comes from the truncations that must be made for tin.

The energy of the two-proton excitation is much lower than twice the shell gap energy due to pairing and  $\alpha$  correlations. For  $^{102}\text{Sn}$ , the two excited protons go into the same deformed quantum states that are occupied by the two valence neutrons. This lowers the energy due to the  $\alpha$ -correlation energy and increases mixing with the neutron configurations near  $N = Z$ . The  $\alpha$  correlation persists for  $^{104}\text{Sn}$  and gradually decreases for increasing number of neutrons since the configurations for the added neutrons differ from the proton configurations. Thus,  $\alpha$  clustering provides a mechanism to generate an asymmetry in the  $B(E2)$  values between  $N = 50$  and  $N = 82$ . Part of the  $\alpha$  clustering could be missed in the ( $t_\pi = 4$ ) calculations due to the seniority truncation that had to be made for tin. In addition, there is an asymmetry-inducing contribution to the  $B(E2)$  values beyond ( $t_\pi = 4$ ) that is obtained in the nickel calculations.

The energy of the low-lying intruder states with  $mp - nh$  configurations is also sensitive to these correlations. The  $2p - 2h$  state in  $^{60}\text{Ni}$  is observed at 3.32 MeV from the  $^{56}\text{Fe}(^6\text{Li}, d)$  reaction [43]. The calculated energy of this state in the full  $pf$  shell model is in agreement with experiment (see Fig. 20 of [44]). In the  $^{100}\text{Sn}$  region,  $2p - 1h$  states have been observed down to  $N = 56$  in the Sb chain as shown in Fig. 3(b). The energies for the  $2p - 1h$   $9/2^+$  levels have been identified and described in [45] for  $^{113-119}\text{Sb}$  nuclei and extended to  $^{107,109}\text{Sb}$  in [46].

For nuclei closer to  $^{100}\text{Sn}$  nothing is known yet. Observation of these states and a comparison to the predictions of the models that include proton excitations are required to complete the understanding of the asymmetry. This prevalence of proton core excitations near  $N = Z$  is also important for understanding the  $B(E2)$  values in  $^{18}\text{O}$ ,  $^{42}\text{Ca}$  and  $^{44}\text{Ca}$  [47, 48] – making the situation en-

countered in the Sn isotopes consistent with observations along proton-magic chains across the nuclear chart.

In summary, we have determined the  $^{104}\text{Sn}$   $B(E2; 0^+ \rightarrow 2_1^+)$  strength from intermediate-energy Coulomb excitation. Our result is at variance with a recently published measurement [1]. Unlike the conclusion of [1], the departure from large-scale shell-model calculations persists for the neutron-deficient Sn isotopes approaching  $^{100}\text{Sn}$ . We propose this deviation from shell model to originate from the interplay of proton particle-hole configurations beyond the necessarily limited shell-model spaces and argue that their effect on quadrupole collectivity is a common phenomenon along proton-magic isotope chains.

This work was supported by the National Science Foundation under Grants No. PHY-1102511, PHY-0606007, and PHY-1068217 and by the US Department of Energy, Office of Nuclear Physics, under Grants No. DE-FG02-08ER41556 and DE-FG02-94ER40834 (U.M.). Support by the Research Council of Norway under contract ISP-Fysikk/216699 is acknowledged. This research used computational resources of the Notur project in Norway.

---

\* Present address: Los Alamos National Laboratory, Los Alamos, NM 87545, USA.

- [1] G. Guastalla *et al.*, Phys. Rev. Lett. 110, 172501 (2013).
- [2] T. Otsuka *et al.*, Phys. Scr. T152 014007 (2013).
- [3] C. Forssen *et al.*, Phys. Scr. T152 014022 (2013).
- [4] C. B. Hinke *et al.*, Nature 486, 341 (2012).
- [5] A. Korgul *et al.*, Eur. Phys. J. A 7, 167 (2000).
- [6] K. L. Jones *et al.*, Nature 465, 454 (2010).
- [7] D. J. Morrissey *et al.*, Nucl. Instrum. Methods in Phys. Res. B 204, 90 (2003).
- [8] D. Bazin *et al.*, Phys. Rev. Lett. 101, 252501 (2008).
- [9] D. Bazin *et al.*, Nucl. Instrum. Methods in Phys. Res. A 606, 314 (2009).
- [10] D. Weisshaar *et al.*, Nucl. Instrum. Methods in Phys. Res. A 624, 615 (2010).
- [11] T. Baugher *et al.*, in preparation.
- [12] T. Motobayashi *et al.*, Phys. Lett. B 346, 9 (1995).
- [13] T. Glasmacher, Annu. Rev. Nucl. Part. Sci. 48, 1 (1998).
- [14] A. Gade and T. Glasmacher, Prog. Part. Nucl. Phys. 60, 161 (2008).
- [15] O. B. Tarasov and D. Bazin, Nucl. Instrum. Methods Phys. Res., Sect. B 266, 4657 (2008), <http://lise.nsl.msu.edu>.
- [16] BNL Evaluated Nuclear Structure Data File (ENSDF), <http://www.nndc.bnl.gov>.
- [17] A. Winther and K. Alder, Nucl. Phys. A 319, 518 (1979).
- [18] A. Gade *et al.*, Phys. Rev. C 68, 014302 (2003).
- [19] A. Ekström *et al.*, Phys. Rev. C 80, 054302 (2009).
- [20] H. Olliver *et al.*, Phys. Rev. C 68, 044312 (2003).
- [21] P. Doornenbal *et al.*, arXiv:1305.2877[nucl-ex] (2013).
- [22] N. Boelaert *et al.*, Phys. Rev. C 75, 054311 (2007).
- [23] J. Cederkäll *et al.*, Phys. Rev. Lett. 98, 17 (2007).
- [24] A. Ekström *et al.*, Phys. Rev. Lett. 101, 1 (2008).
- [25] A. Jungclaus *et al.*, Phys. Lett. B 695, 110 (2011).
- [26] A. Banu *et al.*, Phys. Rev. C 72, 061305 (2005).
- [27] P. Doornenbal *et al.*, Phys. Rev. C 78, 031303 (2008).
- [28] C. Vaman *et al.*, Phys. Rev. Lett. 99, 162501 (2007).
- [29] J. M. Allmond *et al.*, Phys. Rev. C 84, 061303 (2011).
- [30] R. Kumar *et al.*, Phys. Rev. C 81, 024306 (2010).
- [31] D. C. Radford *et al.*, Nucl. Phys. A 757, 264 (2005).
- [32] A. Ekström *et al.*, Phys. Rev. Lett. 110, 192502 (2013).
- [33] D. R. Entem and R. Machleidt, Phys. Rev. C 68, 041001 (2003).
- [34] J. Shergur *et al.*, Phys. Rev. C 71, 064323 (2005) and R. L. Auble, J. B. Ball, and C. B. Fulmer, Nucl. Phys. A 116, 14 (1968).
- [35] G. Hagen *et al.*, Phys. Rev. Lett. 109, 032502 (2012).
- [36] I. Darby *et al.*, Phys. Rev. Lett. 105, 162502 (2010).
- [37] D. Seweryniak *et al.*, Phys. Rev. Lett. 99, 022504 (2007).
- [38] T. Bäck *et al.*, Phys. Rev. C 87, 031306(R) (2013).
- [39] K. L. Yurkewicz *et al.*, Phys. Rev. C 70, 054319 (2004).
- [40] B. A. Brown, Phys. Rev. C 58, 220 (1998).
- [41] E. Chabanat, P. Bonche, P. Haensel, J. Meyer, and R. Schaeffer, Nucl. Phys. A 635, 231 (1998).
- [42] J. Bartel, P. Quentin, M. Brack, C. Guet, and H. B. Hakansson, Nucl. Phys. A 386, 79 (1982).
- [43] H. W. Fulbright *et al.*, Nucl. Phys. A284, 329 (1977).
- [44] M. Honma, T. Otsuka, B. A. Brown and T. Mizusaki, Phys. Rev. C 69, 034335 (2004).
- [45] R. E. Shroy, A. K. Gaigalas, G. Schatz, and D. B. Fossan, Phys. Rev. C 19, 1324 (1979).
- [46] H. Schnare *et al.*, Phys. Rev. C 54, 1598 (1996).
- [47] A. M. Green and W. J. Gerace, Nucl. Phys. A 93, 110 (1967).
- [48] B. H. Flowers and L. D. Skouras, Nucl. Phys. A 136, 353 (1969).